

Foldable-circuit-enabled miniaturized multifunctional sensor for smart digital dust



Chun-Yu You^{1,2,†} , Bo-Fan Hu^{1,2,†}, Bo-Rui Xu¹, Zi-Yu Zhang¹, Bin-Min Wu¹, Gao-Shan Huang^{1,3} , En-Ming Song^{1,2,*} & Yong-Feng Mei^{1,2,3,4,*} 

¹Department of Materials Science & State Key Laboratory of Molecular Engineering of Polymers, Fudan University, Shanghai 200438, People's Republic of China ²Shanghai Frontiers Science Research Base of Intelligent Optoelectronics and Perception, Institute of Optoelectronics, Fudan University, Shanghai 200438, People's Republic of China ³International Institute of Intelligent Nanorobots and Nanosystems, Fudan University, Shanghai 200438, People's Republic of China ⁴Yiwu Research Institute of Fudan University, Yiwu 322000, Zhejiang, People's Republic of China

[†]These authors have equal contributions to this work.

E-mails: sem@fudan.edu.cn (En-Ming Song), yfm@fudan.edu.cn (Yong-Feng Mei)

Cite as: You, C.-Y. et al. Foldable-circuit-enabled miniaturized multifunctional sensor for smart digital dust. *Chip* 1, 100034 (2022). <https://doi.org/10.1016/j.chip.2022.100034>

Received: 12 July 2022

Accepted: 11 November 2022

Published online: 17 November 2022

Smart dust, which refers to miniaturized, multifunctional sensor motes, would open up data acquisition opportunities for Internet of Things (IoT) and Environmental protection applications. However, critical obstacles remain challenging in the integration of high-density sensors, further miniaturization of device platforms, and reduction of cost. Here, we demonstrate the concept of smart digital dust to address these problems, the results of which combine the benefit of (i) maturity of complementary metal-oxide semiconductor (CMOS) processing approaches and (ii) unique form factors of emerging flexible electronics. As a prototype for smart digital dust, we present a millimeter-scale multifunctional optoelectronic sensor platform consisting of high-performance optoelectronic sensor cores and commercially available integrated-circuit components. The smart material-assisted optoelectronic sensing mechanism enables real-time, high-sensitivity hydrogen, temperature, and relative humidity (RH) sensing based on a single chip with ultralow power consumption. Such a microsystem presented here introduces a viable solution to the multifunctional sensing need of IoT and could serve as a building block for the rapidly evolving future framework of smart dust.

Keywords: Smart dust, Flexible electronics, Nanomembrane devices, Multifunctional sensors

INTRODUCTION

Emerging internet of things (IoT) technologies envision a fully connected future^{1,2}. As data becomes the "new oil" of the digital era, the dearth of

data collection techniques, particularly for the diverse data IoT requires, becomes a rising problem. The idea of smart dust in this context, proposed as a sand-grain-scale platform deployed massively into the environment, integrated with sensing, signal processing and communication capabilities³⁻⁵, can exactly handle the data collecting issue. Beginning with initial work of smart dust from almost two decades ago, recently developed work each focus on a single topic, the embodiments range from signal processing⁶⁻⁸ to power management⁹⁻¹¹, and to wireless communication¹²⁻¹⁴. Of particular note is in emerging technologies of microfliers¹⁵, in which bio-inspired 3D morphology brings regulated motion in air, providing a solution to the long-standing challenge of the deployment of a large number of smart dusts^{5,16}.

In spite of the advances achieved in recent years, few microsystems have come close to accomplishing the original vision of smart dust and becoming commercially viable¹¹. Due to the diversity of IoT applications, it is essential to integrate multipurpose sensors and to take a modular approach to reduce design and manufacturing costs. Sensors may work under different principles such as detecting the impedance variance for a metal oxide gas sensor^{17,18} and monitoring the capacitance change of a relative humidity (RH) sensor¹⁹, which complicates the design and hinders miniaturization. Recent works of stacked chips²⁰ and downsizing of functional areas^{13,21} have shown the potential to reduce the system dimension. However, the former increases cost due to the tailor-made assembly and packaging process, while the latter reduces device characteristics due to the increased impact of flicker noise. Consequently, it is difficult to strike a balance between miniaturization, sensor integration, and cost reduction.

To address these problems, we proposed the idea of smart digital dust²², which appears in Fig. 1. In an ideal scenario, the smart digital dust consists of (i) a photovoltaic power input, (ii) a pulse-position modulated optical output, (iii) optoelectronic multifunctional sensors, and (iv) flexible analog and digital circuits, as shown in Fig. 1a. Due to the impracticality of replacing batteries for systems so small and numerous, photovoltaic power inputs will be the ideal option for long-term energy supply²³. Pulse-position modulation of optical output can be generated under low-voltage conditions and delivers the information with high efficiency¹¹. Sensing multiple environmental signals with a single optoelectronic mechanism saves the expense and effort of constructing and installing numerous distinct sensors under varied conditions of IoT^{24,25}. Another feature of importance is the mechanical flexibility for both footprint reduction and manufacturing cost-saving concerns. In the macroscopic domain, folding and rolling are instinctive approaches to reduce footprint size, and they have been proved to be effective in the microscopic and mesoscopic dimensions²⁶⁻²⁸. Therefore, folding the flexible system up reduces the planar

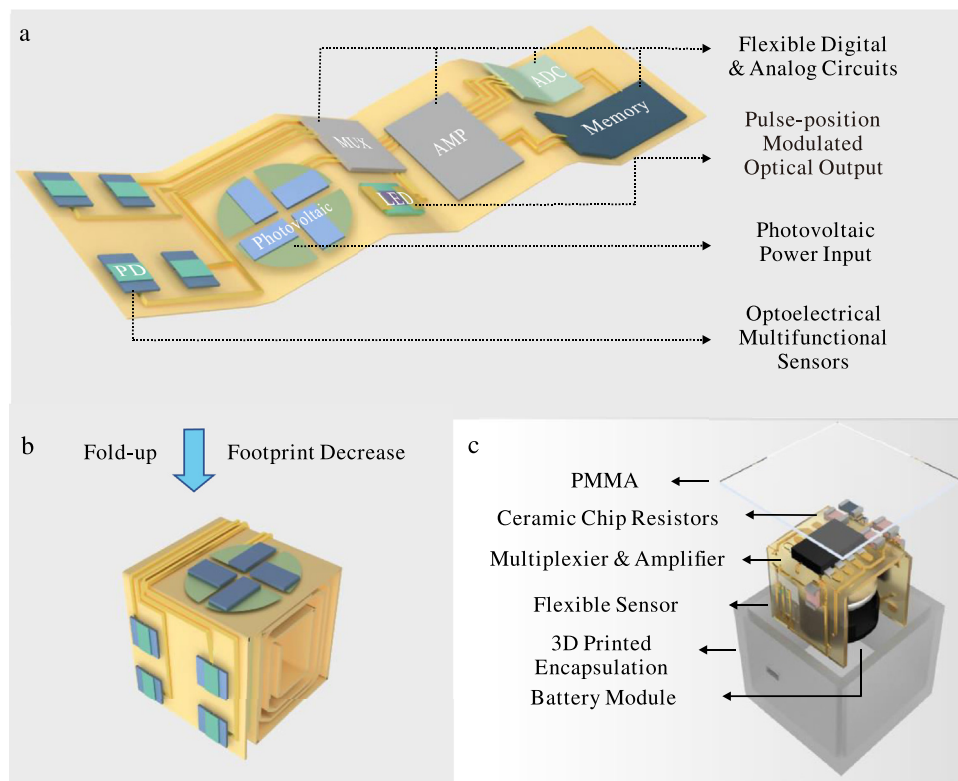


Fig. 1 | Schematics of a fold-up approach to miniaturized smart digital dust footprint. **a**, The essential functional parts of an ideal smart digital dust integrated with full sensing, computing, and communication ability. **b**, Folded-up form of the smart digital dust with reduced volume and intact function. **c**, Exploded-view schematic illustration of the smart digital dust prototype realized upon flexible silicon-nanomembrane optoelectronic sensor array and other commercially available components.

dimensions similar to stacking multiple chips while the majority of the system can be fabricated on the same wafer, as illustrated in Fig. 1b.

This paper presents a millimeter-scale smart digital dust prototype with multifunctional sensing capabilities to demonstrate the viability of the aforementioned concepts. We demonstrate highly flexible silicon nanomembrane transistors decorated with smart materials and achieve low-energy consumption optoelectronic sensing of gas, temperature, and RH. The manufacturing process is complementary metal-oxide semiconductor (CMOS) compatible, and the performance of the resultant transistors is state-of-the-art. We combined our sensor cores with commercially accessible components such as resistors, amplifiers, multiplexers, and batteries to create a flexible circuit. We finish the system by folding the entire circuit and encapsulating it with 3D-printed molds. (Fig. 1c) The system's footprint is minimized, and its real-time, multifunctional sensing performance is uncompromised. The results show the potential of combining the advantages of well-developed CMOS technology and fast-developing flexible electronics to create better IoT devices.

RESULTS AND DISCUSSION

Fig. 2a shows the scheme of the multilayer configuration of the optoelectronic core for multifunctional sensing. The smart materials show transparency or chromatic change to environment change (e.g., humidity, temperature, and specific gas atmosphere), and are decorated on the top of the functional region. A 300-nm thermal oxide derived from the silicon-on-insulator (SOI), serves as an encapsulation for the structure below. The silicon-nanomembrane (Si-NM), stacked gate dielectric and metal contact form the field effect transistor. A spin-coated polyimide buffer, Kwik-Sil

silicone adhesion and a Kapton film supporting layer make up the flexible substrate.

Fig. 2b is a photograph of the fabricated transistor array on a curved tube with a diameter of 5 mm, showing the novel bending ability. Fig. 2c presents the enlarged view of the sensitive region of the transistor. The channel length is 20 μm and the width is 300 μm . Fig. 2d presents schematic illustration of the optoelectronic multifunctional sensing mechanism. The smart materials exhibit chromic or transmittance variation under environment change, thus changing the illumination on the phototransistor beyond. Thereby the environment parameter, e.g., temperature or RH or the concentration of certain gas atmosphere is reflected by the photocurrent. Subsequent analog and digital circuit amplifier the weak current change to a transmissible and voltage signal. Fig. 2e shows output voltage change of the device when 1% hydrogen/nitrogen mixed gas enters the pure nitrogen atmosphere with or without the smart material covering on it. The smart material used here is Pd/MoO₃ bilayer, of which gasochromic performance has been widely studied^{29,30}. When the atmosphere changes, the output voltage of the smart material decorated device rises significantly in just 30 s, whereas the output voltage of the device without smart material decoration remains constant. We will discuss detailed system's characters of the output voltage below and the trend difference here is enough to demonstrate the necessity of smart materials in our optoelectronic sensing. Since the whole detection process occurs in room temperature, this quick detection not only proves the feasibility of optoelectronic sensing mechanism but also demonstrates its potential superiority.

Standard semiconductor processing strategies in pattern defining, growth, etching and transfer printing enable the fabrication of high-quality flexible sensor cores directly from an SOI wafer. Fig. 3a presents critical process of the sensing core, and the details appear in the Methods. Since

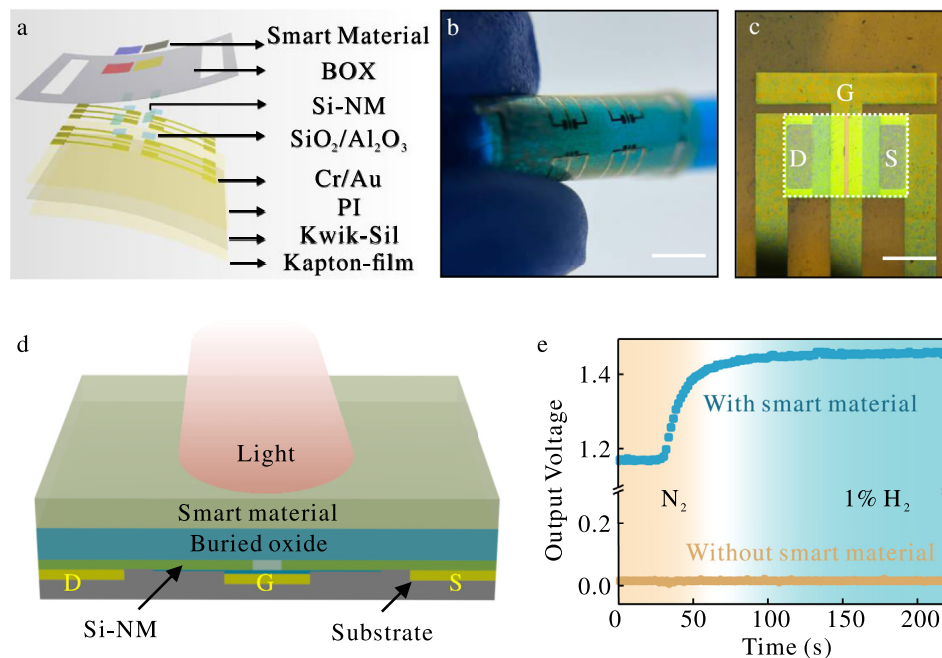


Fig. 2 | Multifunctional sensing core of the smart digital dust based on optoelectronic mechanisms. **a**, Exploded-view schematic illustration of the flexible nanomembrane metal-oxide-semiconductor field effect transistor decorated with diverse stimuli-responsive smart materials. **b**, Photograph of the fabricated flexible phototransistor array on a curved surface. The scale bar is 5 mm. Annotated D, G and S stand for drain, gate, and source terminal of the transistor. **c**, Optical image of a typical phototransistor with a back-gate structure. The scale bar is 200 μm . **d**, The schematic illustration of the sensing mechanism of the smart material assisted multifunctional sensing, in which the chromatic deviation under environment changing is captured by the high-sensitive phototransistor beyond. **e**, Time-dependent performance of the optoelectronic sensor after transimpedance amplify under a hydrogen concentration stimulus in the environment.

the origin wafer is n-type and moderately doped, a boron ion-implantation process forms the source and drain heavily doped region and leaves the channel unchanged for high mobility and easy for gate-tunability concern. Photolithography and reactive ion etching (RIE) isolate the phototransistors preventing signal crosstalk. Gate dielectric is deposited featuring minimal surface states and advanced high-k gate tunability through plasma enhanced chemical vapor deposition (PECVD) and atomic layer deposition (ALD). A lifted-off process forms the metal contact and finish the fabrication of a rigid transistor. By bonding the sample to multilayer flexible substrates and flipping the whole device, inductive-coupled plasma reactive ion etching (ICP-RIE) process etches out the handle layer of the SOI wafer and leaves only the hundreds-nanometer-thick Si-NM and buried oxide (BOX) with the flexible substrate. Finally, different smart materials are decorated onto the flexible transistors, empowering multifunctional sensing on a single chip. Photolithography, ALD and ICP-RIE are typical and standard measures in integrated circuit manufacture, thus ensuring the process compatibility and feasibility towards a larger scale.

Fig. 3b shows transfer characters of a typical phototransistor in the dark at a supply voltage $V_{DS} = -1$ V. The off-current is only at ~ 0.3 pA level and the on-off ratio reaches 10^8 . In addition, Fig. S1 shows transfer characteristics of the phototransistor in the bent state with a curvature of 1 cm^{-1} and flat state, and there is basically no difference between the two. Fig. S2 depicts threshold voltage of the phototransistor after different bending cycles and the threshold voltages show tiny variation. Fig. 3c represents output current at slightly larger V_{DS} , which has the potential to act as the drive current in case the flexible transistors make up an analog or digital circuit in further applications. Since the sensors arrays of smart digital dust are based on optoelectronic sensing mechanisms, optoelectronic performance is crucial to achieve high precision-environment sensing. Fig. 3d

demonstrates transfer curves under different illumination of 450-nm laser at a $V_{DS} = -2$ V. Significant rise of sub-threshold region drain current occurs with only a 60 nW ($0.06\ \mu\text{W}$) laser illumination on the phototransistor. In Fig. 3e, photocurrent of the flexible phototransistor under varying irradiation intensity of the 450-nm laser is plotted ($V_{DS} = -2$ V, $V_{GS} = 1$ V). The phototransistor shows a linear response in a wide range (from ~ 7 nW to ~ 0.1 mW), showing a dynamic range of at least 83 dB.

The electrical performance of each single fabricated sensing core can match the state-of-the-art CMOS counterparts, thus leaving the room to fabricate a whole flexible analog and digital circuit based on the same process used here. And the excellent optoelectronic characteristics of the sensing core not only enable multifunctional environmental sensing, but also consume minimal energy, since it works in the sub-threshold region.

We further integrate the sensing core with commercially available chip components to extend it to a smart digital dust prototype, with various environment sensing abilities and basic signal processing and communication functions. Fig. 4a is a photograph of the smart digital dust prototype next to a coin, showing the miniaturized footprint of millimeter-scale in all three dimensions. Fig. 4b demonstrates a schematic illustration of the electrical operation principle. The whole operation of the smart digital dust can be divided into two parts, which are the on-chip sensing platform and the off-chip signal processing systems. Each of phototransistors, as the photodetector (PD), detects a different environment signal and passes its current to the multiplexer. The transconductance amplifier converts the selected current to a stable voltage signal and passes it to the off-chip system. An analog digital converter (ADC) with a general-purpose input/output (GPIO) transfers the voltage signal to the user interface. The entire system is powered by the battery. Thanks to the development of wearable devices, the design of wireless multifunctional systems has made great progress and has brought inspiration to our system design^{31,32}. The

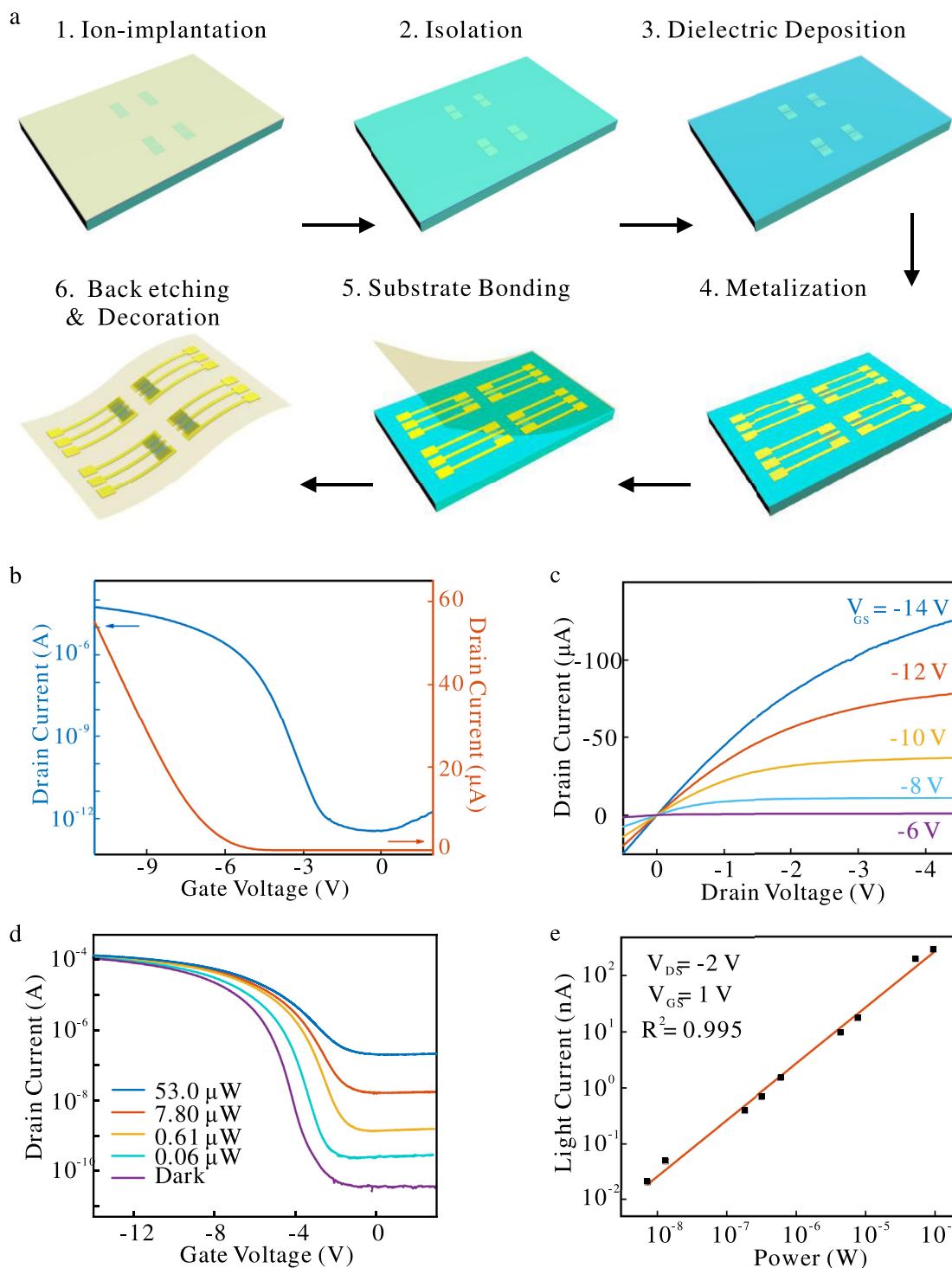


Fig. 3 | CMOS compatible manufacturing process and performance of the smart digital dust sensing core. **a**, Scheme for the crucial steps of fabricating the sensing core utilizing standard integrated circuit process. **b**, The transfer characteristics of a typical phototransistor in dark at a supply voltage $V_{DS} = -1\text{ V}$. **c**, The output characteristics of the device in dark at various V_{GS} . **d**, Drain current-gate voltage relation under different irradiation intensity of a 450-nm laser at a supply voltage (V_{DS}) of -2 V . **e**, Linear response of the device at $V_{DS} = -2\text{ V}$ and $V_{GS} = 1\text{ V}$.

system could be further extended to be totally wireless and Fig. S3 shows a block diagram for a feasible system design.

Fig. 4c-e exemplify the output voltage of the sensing platform under different environment stimuli in constant light condition. The stimuli are a typical gas concentration (i.e., hydrogen here), temperature and

RH. The stimuli-responsive materials used here are the Pd/ WO_3 bilayer for hydrogen concentration, Poly(N-isopropylacrylamide) (PNIPAm) hydrogel for temperature and Poly (2-hydroxyethyl methacrylate-co-acrylic acid) (poly(HEMA-co-AAc)) hydrogel for RH. The transmittance variation of these materials over environment change has been demonstrated

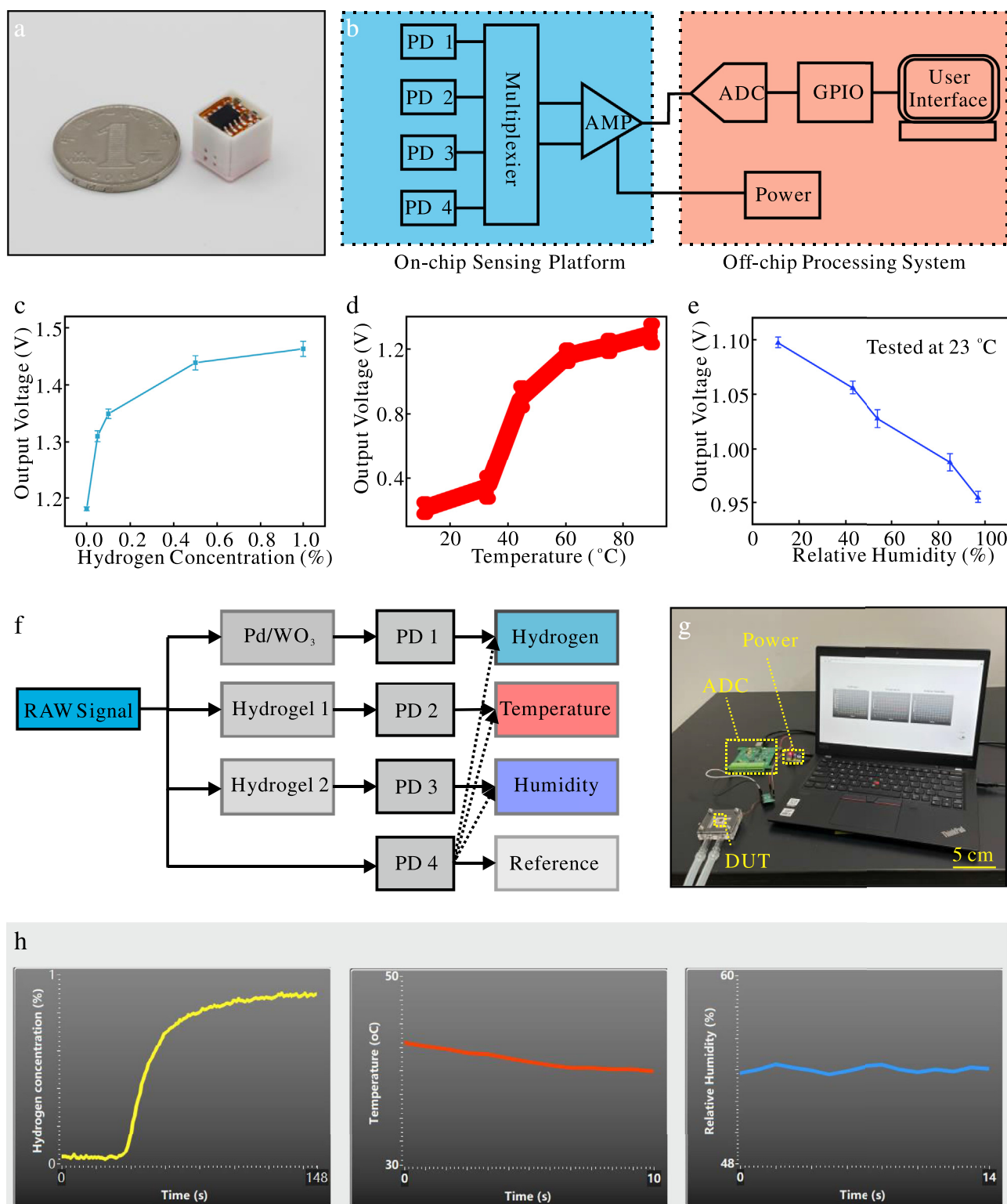


Fig. 4 | Millimeter-scale multifunctional sensing platform. **a**, The photograph of the device beside a coin. **b**, Functional diagram of the platform showing hardware blocks including sensing, signal selection, signal amplifying, power management and data interflow. **c-e**, Variation trend of the output signal under different environment variation which are hydrogen (**c**), temperature (**d**), and relative humidity (**e**). **f**, Schematic illustration of the stimuli-responsive materials assisted optoelectronic operating principles of the platform. Hydrogel 1 stands for PNIPAm and hydrogel 2 is poly(HEMA-co-AAc). **g**, Photograph of the testing scenario, including the ADC, power input and personal computer user interface. **h**, Graphic user interface (GUI) for the multifunctional sensing platform, supporting real-time visualization, storage, and analysis of measurement data.

and their inner mechanism has been discussed thoroughly elsewhere. Fig. S4-6 show the transmittance variation of these smart materials under certain environment stimuli.

For the Pd/WO₃ bilayer smart material, we use for hydrogen sensing, WO₃ is the material that mainly changes light transmittance in a hydrogen-containing environment and Pd acts as a catalyst. The hydrogen gas is dissociated into atomic hydrogen on palladium, which diffuses across the palladium layer and is subsequently inserted into the Pd/WO₃ interface as a hydrogen ion and an electron. With the assistance of one electron from the hydrogen atom, the W⁶⁺ ion in WO₃ is reduced to W⁵⁺. The change of chemical valence of W leads to the change in transmission. For temperature sensing, we use PNIPAm, which is one of the most studied thermosensitive hydrogels. PNIPAm is soluble in water due to its inter- and intramolecular hydrogen bonding in relatively low temperature, thus it is almost transparent. From the thermodynamic point of view, the formation of hydrogen bonds leads to the decrease of mixing enthalpy ($\Delta H_{mix} < 0$), which is conducive to the dissolution process. A highly ordered water molecular layer is formed around the amide group, which reduces the entropy of the system ($\Delta S_{mix} < 0$). At this temperature, $\Delta G_{mix} < 0$, PNIPAm is dissolved in an aqueous solution, where the polymer chain shows a flexible and expanded random coil conformation. When the temperature rises, the hydrogen bonding is weakened, and the hydrophobic interaction between isopropyl groups is enhanced, leading to the decrease of entropy of the mixed system. The change of entropy affects the exothermic enthalpy of hydrogen bonds. When $\Delta G_{mix} > 0$, entropy driven phase separation occurs, PNIPAm chains dehydrate and coalesce into tightly packed spherical conformation, leaving the system opaque. In the case of RH sensing, we exploit the water-absorbing nature of hydrogels and poly(HEMA-co-AAc) is chosen for its high stability and ease to synthesize. There are two types of water absorbed by methacrylate-based hydrogels: free water and bound water. When it is relatively dry, the irregular porous structure of the hydrogel is filled with air. The mismatch between the refractive coefficient of the air and the hydrogel as well as a large number of interfacial interferences during the propagation of transmitted light make the hydrogel appear translucent under dry conditions. With the increase of humidity in the environment, the proportion of water bound in the hydrogel gradually increases, filling the holes originally occupied by air. As water and hydrogel have similar refractive coefficients, they reduce light scattering, increasing overall light transmission.

The output voltage of the platform follows the simple equation as:

$$V_{out} = \frac{V_{cc}}{2} - I \times R \quad (1)$$

where the V_{cc} is the supply voltage of the battery, I is the drain current of the sensing core and R is the resistance of build-out resistor.

As the hydrogen concentration rises, the transmittance of the smart material (Pd/WO₃ bilayer here) decreases^{30,33} as shown in Fig. S4, reducing the output current and causing the output voltage to rise spontaneously, as according to Eq. (1). The temperature sensing scenario is similar since the transmittance lowers drastically as the temperature rises (Fig. S5)^{34,35}. For RH sensing, the hydrogel's transmittance increases as collected water fills its pores and decreases dispersion, which is depicted in Fig. S6^{36,37}. Consequently, the output voltage decreases as RH increases. It should be noted that preventing interaction of RH and temperature sensing is vital. To prevent the interference of RH shift on the temperature sensing, we encapsulate the PNIPAm in the polydimethylsiloxane (PDMS) mold and separate it from the atmosphere, as all hydrogels absorb water from their surroundings³⁸. On the other hand, the interference of temperature shift on the RH sensing do exist. Fig. S7 shows the RH sensing character under different temperature. When temperature rises, the output voltage of our platform do show an increase under the same RH atmosphere. When the

RH is measured by a single smart material and phototransistor combination, an underestimation of RH value could happen at a hot environment. However, since the platform also contains a temperature sensor, this effect could be compensated by adding a feedback circuit or additional software process. Thus, the stability of our temperature sensing could be enhanced.

Using the established relationship, we can carry out real-time environmental parameter sensing. The processes for obtaining the hydrogen concentration, temperature, and RH from the observed data are depicted in Fig. 4f. Each PD adorned with a certain smart material contributes to a particular environmental metric. Since the photocurrent generated by phototransistors is the basis of the sensing process, we employ a PD 4 as a reference to adjust for the environmental light variation. Fig. 4g depicts an image of the testing setup. The device-under-test (DUT) is put in a sealed chamber to provide a certain RH or gas environment. After connecting to the ADC module, the signal from the sensing platform is delivered to the computer, transferred, and displayed as the real-time signal of the environment being evaluated.

Fig. 4h shows the graphic user interface (GUI) of the developed multifunctional sensing platform. The user may monitor the environment signal in real time and adjust the time period to see the change at a certain time interval of interest. The system captures an increase in the hydrogen content, as represented by the yellow line, which includes a surge phase and a slow and steady growing period. The red and blue lines also record the temperature and RH trend over the last 10 s, suggesting a steady RH condition and a gradually dropping temperature near the sensor platform. These results indicate the potential of applying this platform as the sensing element for the multifunctional sensing requirement for IoT applications.

We presented a prototype of smart digital dust using the folded flexible circuit. The sensor core by uses of a bottom-up, back-etching technique that demonstrates superior flexibility and device performance. With rigid processing components and a commercially accessible polyimide substrate, the planer dimensions of the prototype have already been drastically reduced. By constructing the entire system in a flexible manner, the system could be folded more times and the space utilization will reach a higher level.

Compared to the more traditional chip stacking scheme of smart dust, our folding scheme has two advantages: ease of design and low cost. For the chip stacking scheme, size of the chip has a greater impact on its position in the stack combination, rather than depending on function of the chip. The smaller chips are usually required to be stacked on top, while the larger chips are stacked on the bottom. This brings additional difficulties to the interconnection design of the chip. Also, the special design required for stacking chips, the different preparation processes required for different chips, and the need for unconventional manufacturing equipment inevitably bring about an increase in cost. With the folding method, the overall system can be designed like ordinary circuits, and the entire device can be prepared simultaneously in the same batch, which brings higher efficiency and cost advantages.

Multiple sensing functions on a single device, i.e. hydrogen, RH, and temperature sensing, are demonstrated based on optoelectronic mechanism. Since molecular or environmental detection based on visual effect change has been well-established for quite some time, it will only require minimal work to expand sensing capability. Environmental variables such as pH, nitric oxide, and magnetic field are examples of other typical sensing objects³⁹⁻⁴³. However, the purpose of this research is to demonstrate viability of a miniaturized multifunctional sensing platform as a prototype for smart digital dust, and these three sensing functions presented are sufficient for our topic.

In addition, energy input of a tiny system must be limited, thus resource distribution of power consumption is critical. While lowering the power consumption of the analog and digital circuits or the communica-

tion systems would inevitably lower their performance, a suitable outlet is to lower the energy cost of sensors by applying novel sensing mechanisms. In addition, many sensing approaches require heating^{18,44,45}, but it consumes a considerable amount of energy and complicates the integration of the system. Consequently, many sensing mechanisms cannot be used in smart dust systems. Our sensor cores have a power consumption of under 1 nW and their performance does not degrade, satisfying the requirements of IoT applications and making them a great candidate for smart dust.

The presented multifunctional sensing prototype demonstrates the potential of optoelectronic environmental sensing, and with the advancements in components such as signal processing unit, communication system, and vast deployment scheme, the concept of smart digital dust will be realized and serve as the essential core of the IoT era. These microsystems could offer significant opportunities in novel applications like smart homes, digital twins and environmental monitoring. Taking the scenario of environmental-related applications, the temperature and RH data reported by these microsystems could effectively alert or even prevent wildfires, which has become a severe problem recently⁴⁶. And high-precision, large-area greenhouse gas emission mapping may also assist in a wiser judgment regarding the urgent need to achieve carbon neutrality⁴⁷.

METHODS

Fabrication of the sensor core Fabrication began with a commercially available SOI wafer (weakly n-doped; Shanghai Simgui Technology Co. Ltd.), which consisted of a 220-nm top silicon, 300-nm BOX layer and a 725- μm handle substrate. A Boron ion-implantation formed the source and drain region with a doping concentration of $\sim 10^{19} \text{ cm}^{-3}$. Photolithography and RIE defined the Si-NM pattern as the functional region of each phototransistor. PECVD and ALD grew $\text{SiO}_2/\text{Al}_2\text{O}_3$ stack gate dielectric (thickness of 50/15 nm). After opening via through the dielectric at the source and drain region, e-beam evaporation or sputtering grew the Cr/Au metal contact (thickness of 5/150 nm). A buffer layer of polyimide (thickness of $\sim 2 \mu\text{m}$) was spin coated onto the sample, and Kwik-Sil (World Precision Instruments) was used to bond the device to a Kapton film (thickness of $\sim 14 \mu\text{m}$; DuPont). Samples were flipped then, and ICP-RIE process with SF_6/O_2 removed the handle layer of the SOI wafer. Another photolithography and RIE process opened contact windows on the BOX layer and finish the fabrication of sensor cores.

Smart digital dust prototype assembly A Pd/ WO_3 bilayer (5/20 nm) was deposited by e-beam evaporation on a polyethylene film. The PNIPAm preparation started with dissolving 7.91 g of N-isopropylacrylamine, 1.32 g of poly(vinyl alcohol) (PVA), and 215.6 mg (0.0014 mol) of N,N'-methylenebis(acrylamide) into deionized (DI) water. A 520.0 μL aliquot of this solution was pipetted into a centrifuge tube and then 7.0 μL of N,N,N',N'-tetramethylethylenediamine (catalyst) and 16.0 μL of ammonium persulfate (initiator) were added in sequence to the centrifuge tube with vigorous vibration. Then the solution was dropped into a PDMS mold and sealed to protect the PNIPAm. The poly(HEMA-co-AAc) was formed by mixing 4 mL of 2-hydroxyethyl methacrylate, 3 mL of 2-hydroxy-2-methylpropiophenone, and 1 mL of ethylene glycol dimethacrylate together, dropping them between two PDMS molds and ultraviolet curing for 20 s. These smart materials were transferred and decorated onto the sensor cores through a standard transfer printing process. Placing commercially available components according to circuit design, soldering them to the flexible printed circuit boards, folding the system, and encapsulating the system with a 3D printed PVA shell finished assembly. Low-noise precision operational amplify (TLC2201IDR, Texas Instruments)

and high precision low-dropout linear regulator (XC6206P332MR, Torex Semiconductor) as well as matched capacitors and resistors were soldered onto a flexible printed circuit. The system was then folded and encapsulated with a 3D printed PVA shell.

Optoelectronic performance characterization Output and transfer properties were characterized by a precise source meter (Keysight B2902B). Illumination was provided with a semiconductor laser (450-nm; XI'AN Lei Ze Electronic Technology Co. LTD) under the modulation of optical attenuators (Guangzhou Oeabt Optical Technology Co. Ltd.). Irradiation power was calibrated using an optical power meter (Thorlabs PM100D).

Multifunctional sensing test setup Microsystem was placed in a sealed quartz container connected to a gas mixing chamber. Hydrogen atmosphere of different concentrations was obtained by varying the gas flow ratio from the nitrogen gas cylinder and hydrogen/nitrogen mixed gas (0.1%, 1% or 4%) cylinder. Alterable RH was acquired by injecting different saturated salt solutions (K_2CO_3 , NaCl, KCl, and K_2SO_4) into the gas mixing chamber. The corresponding RH values were 43%, 75%, 85%, and 97%, respectively. An additional RH value of 10% was achieved by placing the whole system into a drying cabinet. Temperature-dependent tests were conducted by direct heating the container on the hot plate. Electrical signal was wired to a data acquisition board and then connected to a personal computer. A custom software controlled the system and an oversampling ratio of 16 was used to reduce the noise.

REFERENCE

- Al-Fuqaha, A., Guizani, M., Mohammadi, M., Aledhari, M. & Ayyash, M. Internet of things: a survey on enabling technologies, protocols, and applications. *IEEE Commun. Surv. Tutor.* **17**, 2347–2376 (2015). <https://doi.org/10.1109/comst.2015.2444095>.
- Zanella, A., Bui, N., Castellani, A., Vangelista, L. & Zorzi, M. Internet of things for smart cities. *IEEE Internet Things J.* **1**, 22–32 (2014). <https://doi.org/10.1109/ijot.2014.2306328>.
- Sailor, M. J. & Link, J. R. "Smart dust": nanostructured devices in a grain of sand. *Chem. Commun.* **11**, 1375–1383 (2005). <https://doi.org/10.1039/b417554a>.
- Warneke, B., Last, M., Liebowitz, B. & Pister, K. S. J. Smart Dust: communicating with a cubic-millimeter computer. *Computer* **34**, 44–51 (2001). <https://doi.org/10.1109/2.895117>.
- Kahn, J. M., Katz, R. H. & Pister, K. S. Emerging challenges: mobile networking for "Smart Dust". *J. Commun. Netw.* **2**, 188–196 (2000). <https://doi.org/10.1109/jcn.2000.6596708>.
- Kang, T. et al. A 1.74.12 mm³ fully integrated pH sensor for implantable applications using differential sensing and drift-compensation. In *2019 Symposium on VLSI Circuits*, C310–C311 (IEEE, 2019). <https://doi.org/10.23919/VLSIC.2019.8778184>.
- Chuo, L. X. et al. 7.4 A 915MHz asymmetric radio using Q-enhanced amplifier for a fully integrated 3 \times 3 \times 3 mm³ wireless sensor node with 20 m non-line-of-sight communication. In *2017 IEEE International Solid-State Circuits Conference (ISSCC)*, 132–133 (IEEE, 2017). <https://doi.org/10.1109/isscc.2017.7870296>.
- Chuo, L. X. et al. Millimeter-scale node-to-node radio using a carrier frequency-interlocking if receiver for a fully integrated 4 \times 4 \times 4 mm³ wireless sensor node. *IEEE J. Solid-State Circuits* **55**, 1128–1138 (2019). <https://doi.org/10.1109/JSSC.2019.2959505>.
- Moon, E. et al. Bridging the "last millimeter" gap of brain-machine interfaces via near-infrared wireless power transfer and data communications. *ACS Photon* **8**, 1430–1438 (2021). <https://doi.org/10.1021/acsp Photonics.1c00160>.
- Seo, D. et al. Wireless recording in the peripheral nervous system with ultrasonic neural dust. *Neuron* **91**, 529–539 (2016). <https://doi.org/10.1016/j.neuron.2016.06.034>.
- Molnar, A. C. et al. Nanoliter-scale autonomous electronics: advances, challenges, and opportunities. In *2021 IEEE Custom Integrated Circuits Conference (CICC)*, 1–3 (IEEE, 2021). <https://doi.org/10.1109/CICC51472.2021.9431529>.
- Seo, D., Carmona, J. M., Rabaey, J. M., Maharbiz, M. M. & Alon, E. Model validation of untethered, ultrasonic neural dust motes for cortical recording. *J. Neurosci. Methods* **244**, 114–122 (2015). <https://doi.org/10.1016/j.jneumeth.2014.07.025>.
- Cortese, A. J. et al. Microscopic sensors using optical wireless integrated circuits. *Proc. Natl. Acad. Sci. U.S.A.* **117**, 9173–9179 (2020). <https://doi.org/10.1073/pnas.1919677117>.

14. Lee, S. et al. A 250 $\mu\text{m} \times 57 \mu\text{m}$ microscale opto-electronically transduced electrodes (motes) for neural recording. *IEEE Trans. Biomed. Circuits Syst.* **12**, 1256–1266 (2018). <https://doi.org/10.1109/TBCAS.2018.2876069>.
15. Kim, B. H. et al. Three-dimensional electronic microfilers inspired by wind-dispersed seeds. *Nature* **597**, 503–510 (2021). <https://doi.org/10.1038/s41586-021-03847-y>.
16. Barker, J. & Barmoutis, A. Smart dust: Monte Carlo simulation of self-organised transport. *J. Comput. Electron.* **3**, 317–321 (2004). <https://doi.org/10.1007/s10825-004-7068-3>.
17. Korotcenkov, G. & Cho, B. K. Metal oxide composites in conductometric gas sensors: achievements and challenges. *Sens. Actuators B Chem.* **244**, 182–210 (2017). <https://doi.org/10.1016/j.snb.2016.12.117>.
18. Kim, J.-H., Mirzaei, A., Kim, H. W. & Kim, S. S. Flexible and low power CO gas sensor with Au-functionalized 2D WS₂ nanoflakes. *Sens. Actuators B Chem.* **313** (2020). <https://doi.org/10.1016/j.snb.2020.128040>.
19. Farahani, H., Wagiran, R. & Hamidon, M. N. Humidity sensors principle, mechanism, and fabrication technologies: a comprehensive review. *Sensors* **14**, 7881–7939 (2014). <https://doi.org/10.3390/s140507881>.
20. Oh, S. et al. IoT² — the Internet of Tiny Things: realizing mm-scale sensors through 3D die stacking. In *2019 Design, Automation & Test in Europe Conference & Exhibition (DATE)*, 686–691 (IEEE, 2019). <https://doi.org/10.23919/DATE.2019.8715201>.
21. Miskin, M. Z. et al. Electronically integrated, mass-manufactured, microscopic robots. *Nature* **584**, 557–561 (2020). <https://doi.org/10.1038/s41586-020-2626-9>.
22. Li, G. et al. Silicon nanomembrane phototransistor flipped with multifunctional sensors toward smart digital dust. *Sci. Adv.* **6**, eaaz6511 (2020). <https://doi.org/10.1126/sciadv.aaz6511>.
23. Kim, T. S., Kim, H. J., Han, J.-H., Choi, W. J. & Yu, K. J. Flexible InGaP/GaAs tandem solar cells encapsulated with ultrathin thermally grown silicon dioxide as a permanent water barrier and an antireflection coating. *ACS Appl. Energy Mater.* **5**, 227–233 (2022). <https://doi.org/10.1021/acsaem.1c02764>.
24. Rakow, N. A. & Suslick, K. S. A colorimetric sensor array for odour visualization. *Nature* **406**, 710–713 (2000). <https://doi.org/10.1038/35021028>.
25. Wang, C. et al. User-interactive electronic skin for instantaneous pressure visualization. *Nat. Mater.* **12**, 899–904 (2013). <https://doi.org/10.1038/nmat3711>.
26. Zhu, M. & Schmidt, O. G. Tiny robots and sensors need tiny batteries—here's how to do it. *Nature* **589**, 195–197 (2021). <https://doi.org/10.1038/d41586-021-00021-2>.
27. Huang, G. S. & Mei, Y. F. Assembly and self-assembly of nanomembrane materials—from 2D to 3D. *Small* **14**, 1703665 (2018). <https://doi.org/10.1002/smll.201703665>.
28. Zhang, Z., Tian, Z., Mei, Y. F. & Di, Z. Shaping and structuring 2D materials via kirigami and origami. *Mater. Sci. Eng. R Rep.* **145** (2021). <https://doi.org/10.1016/j.mser.2021.100621>.
29. Lee, Y.-A., Kalanur, S. S., Shim, G., Park, J. & Seo, H. Highly sensitive gasochromic H₂ sensing by nano-columnar WO₃-Pd films with surface moisture. *Sens. Actuators B Chem.* **238**, 111–119 (2017). <https://doi.org/10.1016/j.snb.2016.07.058>.
30. Lee, S.-H. et al. Raman spectroscopic studies of gasochromic α -WO₃ thin films. *Electrochim. Acta* **46**, 1995–1999 (2001). [https://doi.org/10.1016/s0013-4686\(01\)00379-6](https://doi.org/10.1016/s0013-4686(01)00379-6).
31. Sang, M. et al. Ultrahigh sensitive Au-doped silicon nanomembrane based wearable sensor arrays for continuous skin temperature monitoring with high precision. *Adv. Mater.* **34**, 2105865 (2022). <https://doi.org/10.1002/adma.202105865>.
32. Kang, K., Park, J., Kim, K. & Yu, K. J. Recent developments of emerging inorganic, metal and carbon-based nanomaterials for pressure sensors and their healthcare monitoring applications. *Nano Res.* **14**, 3096–3111 (2021). <https://doi.org/10.1007/s12274-021-3490-0>.
33. Mirzaei, A., Kim, J.-H., Kim, H. W. & Kim, S. S. Gasochromic WO₃ nanostructures for the detection of hydrogen gas: an overview. *Appl. Sci.* **9**, 1775 (2019). <https://doi.org/10.3390/app9091775>.
34. Roy, D., Brooks, W. L. A. & Sumerlin, B. S. New directions in thermoresponsive polymers. *Chem. Soc. Rev.* **42**, 7214–7243 (2013). <https://doi.org/10.1039/C3CS35499G>.
35. Zhou, Y., Cai, Y. F., Hu, X. & Long, Y. Temperature-responsive hydrogel with ultra-large solar modulation and high luminous transmission for “smart window” applications. *J. Mater. Chem. A* **2**, 13550–13555 (2014). <https://doi.org/10.1039/c4ta02287d>.
36. Zhu, H. et al. Self-powered locomotion of a hydrogel water strider. *Sci. Robot.* **6**, eabe7925 (2021). <https://doi.org/10.1126/scirobotics.abe7925>.
37. Hyon, S.-H., Cha, W.-I. & Ikada, Y. Preparation of transparent poly (vinyl alcohol) hydrogel. *Polym. Bull.* **22**, 119–122 (1989). <https://doi.org/10.1007/BF00255200>.
38. Zhang, Y. S. & Khademhosseini, A. Advances in engineering hydrogels. *Science* **356**, eaaf3627 (2017). <https://doi.org/10.1126/science.aaf3627>.
39. Shi, M. et al. Transparent and flexible structurally colored biological nanofiber films for visual gas detection. *Matter* **5**, 2813–2823 (2022). <https://doi.org/10.1016/j.matt.2022.05.043>.
40. He, L. & Yin, Y. Magnetically responsive photonic nanostructures: making color using magnets. *Proc. SPIE* **8031**, 80310U (2011). <https://doi.org/10.1117/12.884697>.
41. Kim, I. et al. Holographic metasurface gas sensors for instantaneous visual alarms. *Sci. Adv.* **7**, eabe9943 (2021). <https://doi.org/10.1126/sciadv.abe9943>.
42. Qin, M. et al. Bioinspired hydrogel interferometer for adaptive coloration and chemical sensing. *Adv. Mater.* **30**, 1800468 (2018). <https://doi.org/10.1002/adma.201800468>.
43. Park, J. et al. Therapeutic-gas-responsive hydrogel. *Adv. Mater.* **29**, 1702859 (2017). <https://doi.org/10.1002/adma.201702859>.
44. Ren, Y. et al. Synthesis of orthogonally assembled 3D cross-stacked metal oxide semiconducting nanowires. *Nat. Mater.* **19**, 203–211 (2020). <https://doi.org/10.1038/s41563-019-0542-x>.
45. Ma, J. et al. Pt nanoparticles sensitized ordered mesoporous WO₃ semiconductor: gas sensing performance and mechanism study. *Adv. Funct. Mater.* **28** (2017). <https://doi.org/10.1002/adfm.201705268>.
46. Garcia, L. C. et al. Record-breaking wildfires in the world's largest continuous tropical wetland: integrative fire management is urgently needed for both biodiversity and humans. *J. Environ. Manage.* **293**, 112870 (2021). <https://doi.org/10.1016/j.jenvman.2021.112870>.
47. Wang, F. et al. Technologies and perspectives for achieving carbon neutrality. *Innovation* **2**, 100180 (2021). <https://doi.org/10.1016/j.xinn.2021.100180>.

MISCELLANEA

Supplementary materials Supplementary material associated with this article can be found, in the online version, at doi:10.1016/j.chip.2022.100034.

Acknowledgment This work is supported by the National Key Technologies R&D Program of China (2021YFE0191800), the National Natural Science Foundation of China (61975035, 51961145108), and Science and Technology Commission of Shanghai Municipality (21142200200, 20501130700). E.S. acknowledged the support by Lingang Laboratory (Grant No. LG-QS-202202-02), the support by Shanghai Municipal Science and Technology Major Project (Grant No. 2018SHZDZX01), ZJ Lab, and Shanghai Center for Brain Science and Brain-Inspired Technology, and the support by the young scientist project of MOE innovation platform, Zhangjiang Fudan International Innovation Center. Part of the experimental work was carried out in Fudan Nanofabrication Laboratory.

Declaration of Competing Interest The authors declare no competing interests.

© 2022 The Author(s). Published by Elsevier B.V. on behalf of Shanghai Jiao Tong University. This is an open access article under the CC BY-NC-ND license (<http://creativecommons.org/licenses/by-nc-nd/4.0/>)